Journal of Power Sources 216 (2012) 345–352

Contents lists available at SciVerse ScienceDirect

Journal of Power Sources

journal homepage: www.elsevier.com/locate/jpowsour

Experimental study of an air-cooled thermal management system for high capacity lithium–titanate batteries

Michael R. Giuliano*, Ajay K. Prasad, Suresh G. Advani

Center for Fuel Cell Research, Department of Mechanical Engineering, University of Delaware, Newark, DE 19716, USA

HIGHLIGHTS

- ► An air-cooled system to maintain safe Li-ion battery operating temperatures was designed.
- ► The role of state-of-charge on battery thermal behavior was identified.
- ► Li-ion battery cooling with ambient air is a viable solution.
- ► This design is more energy efficient than traditional liquid-cooled designs.

ARTICLE INFO

Article history:
Received 21 February 2012
Received in revised form
24 May 2012
Accepted 25 May 2012
Available online 1 June 2012

Keywords:
Battery electric vehicle
Hybrid electric vehicle
Lithium–titanate battery
Metal foam heat exchanger
Thermal analysis
Battery cooling

ABSTRACT

Lithium–titanate batteries have become an attractive option for battery electric vehicles and hybrid electric vehicles. In order to maintain safe operating temperatures, these batteries must be actively cooled during operation. Liquid-cooled systems typically employed for this purpose are inefficient due to the parasitic power consumed by the on-board chiller unit and the coolant pump. A more efficient option would be to circulate ambient air through the battery bank and directly reject the heat to the ambient. We designed and fabricated such an air-cooled thermal management system employing metal-foam based heat exchanger plates for sufficient heat removal capacity. Experiments were conducted with Altairnano's 50 Ah cells over a range of charge-discharge cycle currents at two air flow rates. It was found that an airflow of 1100 mls^{-1} per cell restricts the temperature rise of the coolant air to less than 10 °C over ambient even for 200 A charge-discharge cycles. Furthermore, it was shown that the power required to drive the air through the heat exchanger was less than a conventional liquid-cooled thermal management system. The results indicate that air-cooled systems can be an effective and efficient method for the thermal management of automotive battery packs.

1. Introduction

Battery electric vehicles (BEV's) and hybrid electric vehicles (HEV's) employ battery packs and electric motors to improve vehicle efficiency and performance by replacing or supplementing traditional drivetrains. The battery faces a challenging set of demands including high energy density, the ability to tolerate large charge and discharge currents, and long cycle life. Various battery chemistries and electrolyte materials have been developed previously that delivered acceptable performance but often suffered from significant disadvantages such as memory effects or thermal runaway. Recently, lithium–titanate battery technology has demonstrated good performance and excellent cycle life without the typical concerns about battery safety [1]. However, due to their exposure to high C-rates and the resulting internal heat generation especially under an urban transit drive cycle, thermal management of these battery packs must be carefully addressed. Maintaining cell temperatures in the optimal range is necessary to ensure safe operation and prolong battery life.

The batteries used in this study are 50 Ah lithium–titanate cells produced by Altairnano [2]. They have an operating voltage range of 1.81–2.79 V and can withstand charge and discharge currents of over 400 A. Their nanostructured anode and cathode materials eliminate concerns regarding thermal runaway, and testing has shown that they do not suffer from memory effects [1]. These cells have a maximum operating temperature of 55 °C and our initial experiments have revealed that this temperature limit can be reached very quickly in the absence of an active thermal management system.

* Corresponding author. Tel.: +1 302 831 4064; fax: +1 302 831 3619.
E-mail address: mgiuliano01@gmail.com (M.R. Giuliano).

0378-7753/$ – see front matter © 2012 Elsevier B.V. All rights reserved.
http://dx.doi.org/10.1016/j.jpowsour.2012.05.074

Previously, we showed that a liquid-cooled thermal management system is a viable option for the active cooling of lithium–titanate batteries [3]. It was also realized that any liquid-cooled system potentially requires a substantial amount of power to operate. Traditional liquid-cooled designs incorporate a closed loop system in which the active fluid would absorb heat from the batteries and reject it to the ambient by means of an on-board chiller unit. In addition, a pump would also be required to circulate the fluid at the desired mass flow rate. The resulting parasitic power losses, as well as the added weight and volume of these on-board components, would reduce the overall efficiency of the EV. The desire to provide safe operating temperatures with a system that minimizes parasitic power losses has motivated the current design and implementation of a thermal management system that utilizes ambient air as the coolant fluid. The obvious concern with such an open-loop system is its loss of effectiveness when operating in hot ambient conditions. It was recognized that the heat exchanger plates would have to be designed carefully in order to ensure adequate heat removal from the batteries even under the most stringent ambient conditions.

Other studies have shown through modeling that air can be an effective medium for thermal management for certain cell geometries [4]. These studies, however, do not contain experimental verification of their results. Hence, the actual implementation of an air-cooled system was explored in this study. We describe the procedures used to design and test an air-cooled thermal management system under laboratory conditions and draw conclusions about its effectiveness. In addition, our experimental results provided insight into the effect of cell state-of-charge on internal resistance and thus overall thermal behavior.

2. Heat exchanger plate design

The liquid-cooled system described in [3] provided valuable data that proved useful in the design of an air-cooled system. At 200 A of charge current, the heat generated by each cell is calculated as approximately 40 W, which served as a suitable target for assessing the feasibility of various designs. These values replicate actual operating conditions in which the batteries operate under large current demands. It was apparent that simply creating a gap between adjacent cells and blowing ambient air through it would not provide an adequate convective heat transfer coefficient to effectively remove the heat from the cells, especially under hot ambient conditions. For this reason the design had to incorporate a method to increase the effective heat transfer coefficient across the face of the cells. Accordingly, a heat-exchanger plate was designed that incorporated a panel of open-cell aluminum foam placed between adjacent cells. To manage the direction of air travel and to protect the surface of the battery from damage, an aluminum encasement was constructed to house the porous medium. This design is shown in Fig. 1.

In order to distribute the air evenly between cells, a manifold was constructed from aluminum box channel. The manifold was fitted with a thermistor and pressure gauge to monitor the temperature and pressure of the incoming air. A rubber air hose was used in conjunction with barbed pipe fittings to connect the manifold to each cooling plate. The air flow rate was controlled with a regulator on the compressed air line in the lab and monitored with a rotameter installed upstream of the manifold.

Given the design constraints of our application, it was necessary to select aluminum foam with the optimal specifications. Open cell porous media are defined by their material of construction, relative density, and pore size defined in terms of pores-per-inch (PPI). Based on physical space limitations of the battery compartment the gap between each cell must be 9.5 mm. Accordingly, the optimal

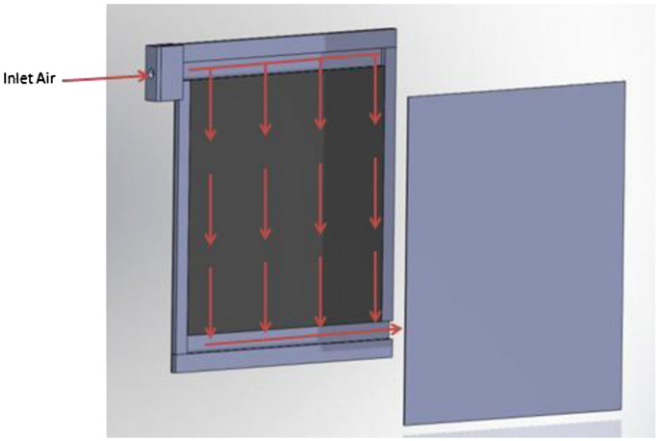

Fig. 1. Exploded view of the assembly. The black panel represents the aluminum foam while the red arrows show the direction of air flow. The air inlet is located at the top to match the region of the cell with the highest heat generation rate. The aluminum foam is sandwiched between aluminum sheets (1.27 mm thick) to complete the encasement. (For interpretation of the references to color in this figure legend, the reader is referred to the web version of this article.)

pore size was determined to be 1.3 mm, thus allowing seven pores to exist across the gap between adjacent cells. In order to determine the optimal density the chart in Fig. 2, published by ERG Duocel, was used.

From Fig. 2 it is clear that the power required to drive a desired airflow through aluminum foam with a relative density of 8% would be very small compared to the other two higher density foams, making it a suitable choice for our application. At the lowest density of 8%, a higher flow rate could be employed to increase the effective heat transfer coefficient while still limiting the pressure drop across the foam and the power required to operate the system. A close-up image of the aluminum foam is shown in Fig. 3.

Prior to construction, calculations were conducted to confirm that the theoretical level of cooling was sufficient for effective thermal management of the cells in a worst case scenario. These heat transfer calculations are outlined next. First, the required theoretical heat transfer coefficient, h, was calculated as

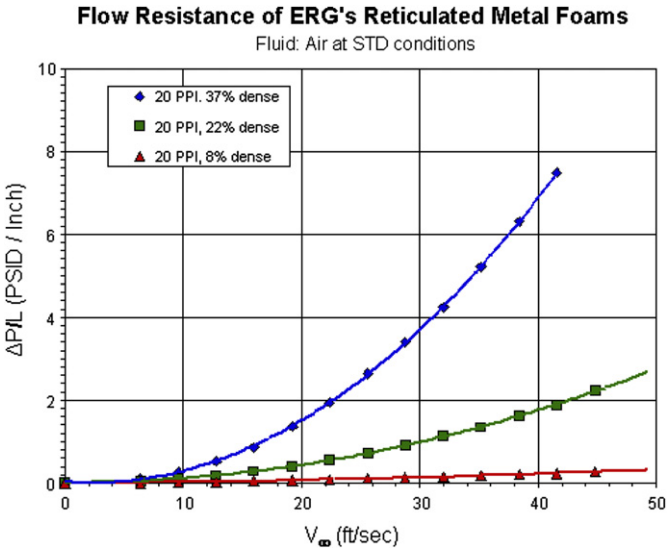

Fig. 2. Pressure gradient vs. velocity for aluminum foam with 20 pores per inch and various densities [5]. These data were used to determine the power required to drive the blower at the desired flow rate.

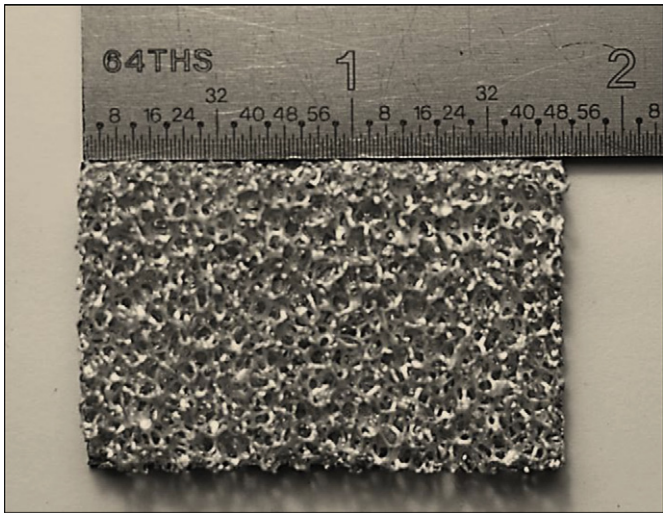

Fig. 3. A close-up of 20 PPI, 8% dense aluminum foam (ruler alongside shows inches). This foam, represented by the black region in Fig. 1, acts as the medium to increase the effective heat transfer coefficient within each heat exchanger plate.

$$h = \frac{q}{A\Delta T} \tag{1}$$

where q is known to be 40 W at 200 A, A is the surface area of the cell, and ΔT is the temperature difference between inlet air and the surface of the cell. To obtain a conservative estimate, q is set to 50 W, and ΔT to 10 °C. The surface area of the cell is equal to

$$A = 0.20{*}0.22{*}2 = 0.088\ \mathrm{m}^2 \tag{2}$$

where the multiplier of 2 accounts for the surfaces on both sides of the cell. Equations (1)–(2) then yield a heat transfer coefficient of 56.5 W m^{-2} C^{-1}. Finally, the procedure outlined in [6] was followed to ensure this value could be achieved. The calculations are shown below in Equations (3)–(5):

$$h = \sqrt{3\pi}\left(\frac{k_s}{a}\right)\left[CPr^{\frac{1}{3}}\left(\frac{k_f}{k_s}\right)\right]^{\frac{1}{2}}\left[\frac{aV_f}{\nu_f}\right]^{\frac{n}{2}}\left[\frac{\rho^{\frac{1}{2}}}{\left(\frac{a}{d}-1\right)^{\frac{n}{2}}}\right] \tag{3}$$

where k_s and k_f are the thermal conductivities of the solid and fluid respectively, a is the pore size, Pr is the dimensionless Prandtl number, V_f is the fluid velocity, ν_f is the kinematic viscosity of the fluid, ρ is the relative density of the metal foam, d is the predicted diameter of the spinels that connect each pore, and C and n are constants based on Reynolds number and the geometric characteristics of the porous media. The following equations describe relative density, ρ, and the estimation for the spinel diameter, d:

$$\rho = \frac{\rho^*}{\rho_s} \tag{4}$$

where ρ^* is the density of the porous media, and ρ_s is the density of a solid block of the same material and volume.

$$d \approx a\left(\frac{2}{\sqrt{3\pi}}\right)\rho^{\frac{1}{2}} \tag{5}$$

Here, a is the pore size, and ρ is relative density as defined in Equation (4).

The results in Table 1 are for two different airflow rates, each yielding heat transfer coefficients within an acceptable range. The author in [6] also states that the theoretical values for heat transfer coefficient are often significantly higher than measured values due to simplifications in the model. In order to obtain accurate values for pressure drop across the porous media and corresponding parasitic power loss, the pressure of the inlet air reported in Table 1 was measured for each flow rate experimentally. Parasitic power was computed using:

$$\text{Power} = Q{*}\Delta P \tag{6}$$

where Q is volumetric flow rate, and ΔP is pressure drop across the metal foam. With the theoretical results showing promising values for both the heat transfer coefficient and parasitic power consumption, the air-cooled system was constructed.

3. Fabrication

The testing of the air-cooled system was conducted with the same experimental set up as described in [3]. Thermochromic liquid crystal (TLC) thermography was again employed to determine the surface temperature distribution of the front-most cell in the 5-cell stack. A heat-exchanger plate was placed in between adjacent cells, leading to the assembly shown in Fig. 4. Each heat-exchanger plate consisted of a sheet of aluminum foam within an aluminum encasement as described earlier in Section 1. Aluminum foam with 20 PPI and 8% relative density was custom ordered from ERG Duocel to fit the dimensions 4.77 mm × 177 mm × 222 mm. The front and back aluminum plates that sandwich the foam measured 1.27 mm thick. This plate thickness was selected to minimize thermal resistance and to promote ease of construction. The entire assembly required complete air sealing in addition to mechanical robustness so tungsten inert gas welding was chosen to fasten the design together. This is a tedious process and therefore would not be a reasonable choice for full-scale production. However, this option sufficed for the small number of plates needed in this project. The TLC strips placed on the front of the stack provided continuous temperature measurements on the surface of the cell throughout the duration of the experiments.

In order to promote efficient heat transfer between the cooling plates and the cells a method for compressing the assembly of cells was created. This fixture needed to be very rigid and cover the entire surface area of the cell while still allowing optical access to the TLC strips via the camera. To accomplish this, a 12.7 mm thick steel cover plate was used that included a milled viewing window, and eight holes for threaded rods. This design is shown in Fig. 5. The cross section of the assembly of cells and cooling plates is shown in Fig. 6 with the compression plates at the front and the back. The insulating material on the front of the stack is the double-paned Plexiglas fixture that was used in [3]. Plywood was used as the insulating material on the back of the stack.

Die springs were employed to accurately control the amount of compression applied to the stack. The springs slide over each of the eight threaded rods that are situated along the left and right borders of the compression plate as shown in Fig. 5. The force exerted by each spring can be determined as the product of its deflection, x, and the spring constant, k:

Table 1
Pressure drop (experimentally measured), heat transfer coefficient (calculated from Equation (3)), and parasitic power required to achieve the two prescribed air flow rates per heat-exchanger plate assembly (from Equation (6)).

Q(mls^{-1})	ΔP (Pa)	h (W m^{-2} K^{-1})	Parasitic power (W)
1100	5171	90.44	5.69
800	3447	80	2.76

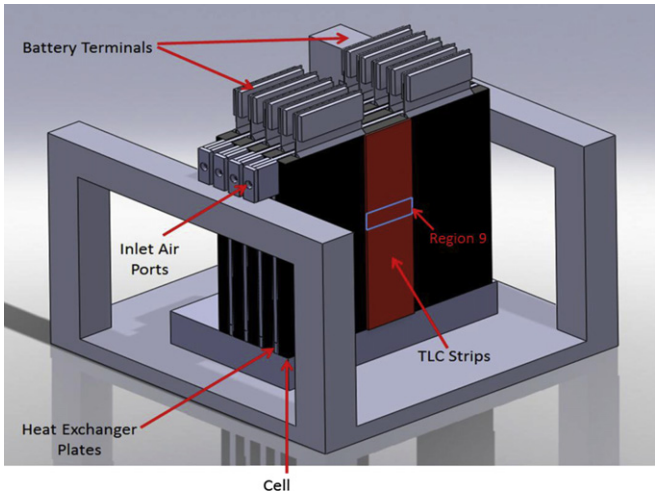

Fig. 4. Solid model of the battery pack with cooling plates inserted between adjacent cells in the testing stand. Region 9 marks the location of the temperature measurements in the graphs in Sections 4 and 5.

$$F = -kx \tag{7}$$

Springs were ordered with a spring constant of 174.8 N cm^{-1} with a maximum force of 266.4 N, which when multiplied by a total of eight springs, supplied adequate compressive force for this application. The springs also allowed for the thermal expansion of the batteries and cooling plates during charge/discharge cycling. This eliminates the development of uncontrolled thermal stresses on the cells as they approach their maximum temperature and avoids the possibility of permanent cell damage. In compliance with specifications from Altairnano the applied compression force on the cells was kept below 1776 N.

A schematic of the complete testing system is shown in Fig. 7. With the air cooling assembly constructed, a testing procedure was implemented to quantify the effectiveness of the system.

4. Effect of SOC on battery thermal behavior

Through initial testing it was discovered that the thermal behavior of the battery was highly dependent on its state-of-charge. Fig. 8, acquired from Altairnano, describes internal impedance versus state-of-charge (SOC) for both charge and discharge currents. Fig. 8 reveals that during low SOC (high states-of-discharge) the cell's internal resistance during discharge cycles is approximately 50% higher than during charge cycles. On the other hand, the internal impedance of the cell is essentially independent of current direction during high SOC.

The primary mechanism of heat generation is due to the battery's internal resistance as given by

$$P = I^2R \tag{8}$$

Due to the linear dependence of P on R, at low SOC the heat generated during discharge is expected to be 50% higher than the heat generated during charge. In contrast, the heat generation is expected to be independent of current direction at high SOC. In order to illustrate this phenomenon experimentally a trial was

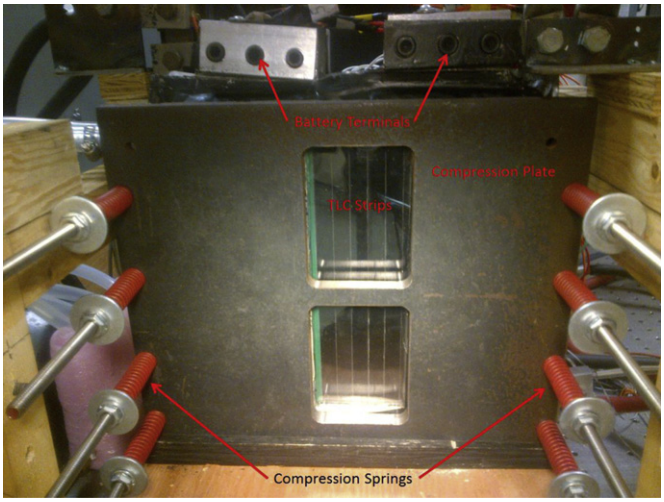

Fig. 5. Experimental setup showing the compression arrangement. The steel compression plate has two windows milled into it for visual access to the TLC strips. Compression springs inserted over lengths of threaded rod are used to adjust the compression force exerted on the cells.

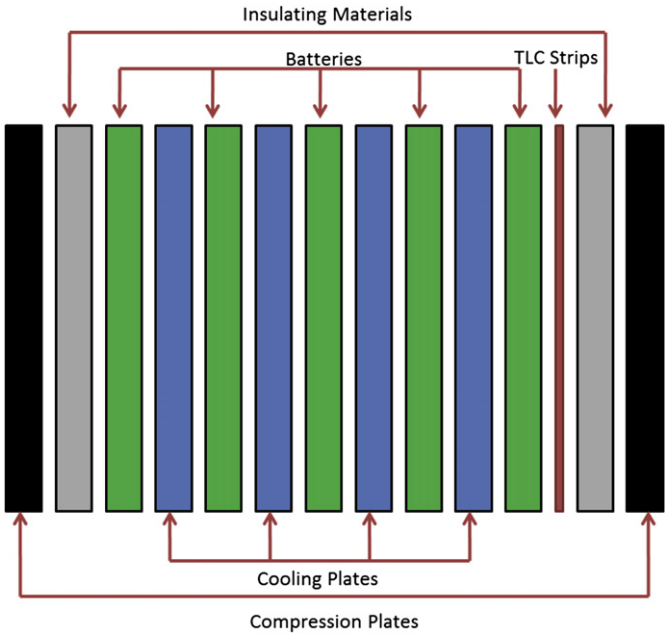

Fig. 6. Schematic of the cross section of the entire assembly (thickness direction). The front of the stack is on the right side, as indicated by the location of the TLC strips.

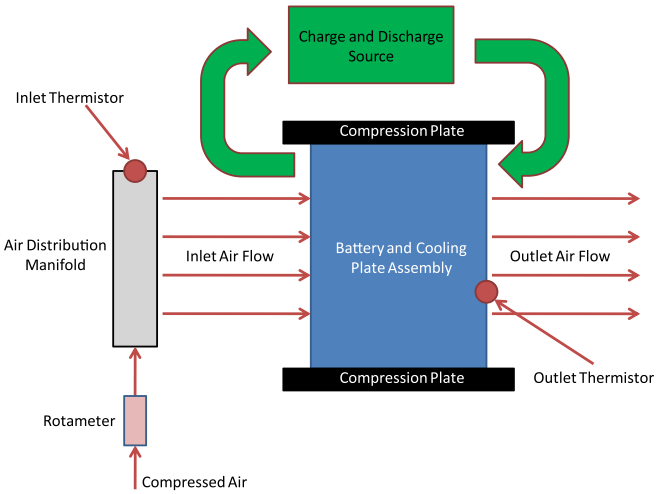

Fig. 7. Schematic of the air-cooled system showing coolant flow configuration and measurement devices for battery testing.

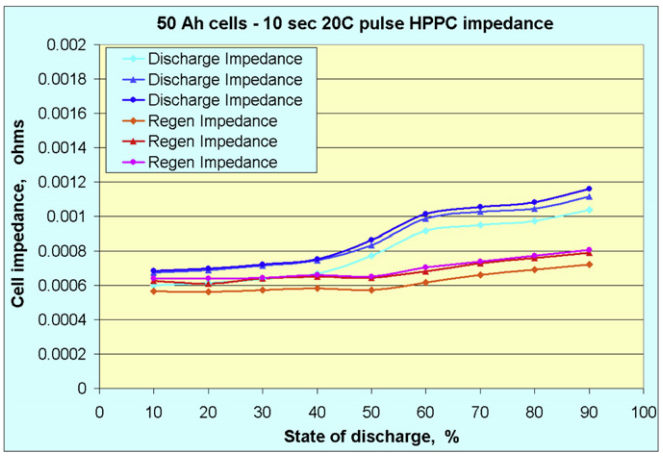

Fig. 8. The difference in internal impedance during charge and discharge cycles is significant at low states-of-charge. Therefore at low SOC, battery thermal behavior is a function of state-of-charge.

conducted at 175 A at both low and high SOC (Fig. 9). As SOC varies linearly with cell voltage, the battery SOC % was determined as follows:

$$\mathrm{SOC} = \frac{(V_{Avg} - V_{MIN})}{(V_{MAX} - V_{MIN})} * 100 \quad (9)$$

where V_{Avg} is the average cell voltage for all the cells in the stack, V_{MIN} is 1.81 V and V_{MAx} is 2.79 V.

The cells were operated using 5-min charge and discharge cycles for the duration of the experiment. The results from this trial are displayed in Fig. 9. It is seen that the temperature profile during charge-discharge cycling exhibits large periodic fluctuations only at low SOC (up to 90 min) for which the internal resistance during discharge is substantially higher than during charge. It is also interesting to note that the temperature fluctuations are perfectly negatively correlated to the SOC fluctuations. As the battery SOC climbs (i.e. charging) the cell resistance is low, and the heat generation rate is smaller than the heat removal rate, due to which the cell temperature falls. During discharging, the battery SOC drops while the heat generation rate climbs faster than the heat removal rate leading to a positive temperature excursion. At 90 min, the battery SOC is increased to values exceeding 50%, and the temperature fluctuations vanish as expected because the internal resistances during charge and discharge converge to the same value at high SOC as indicated in Fig. 7, and the heat removal rate matches the heat generation rate. Such steady-state conditions are preferable for battery thermal analysis, and hence, all further testing was conducted at high SOC.

Under typical operating conditions the batteries experience current demands between 100 and 200 A. For this reason these two current values were selected for comprehensive testing. The testing procedure outlined in [3] was also applied to the air-cooled system. Thus, the stack was exposed to 5 min charge and discharge cycles until a steady-state temperature was reached. In addition, active surface temperature measurements were resolved using thermochromic liquid crystal thermography as described in detail in [3] to an accuracy of ±0.5 °C.

5. Results

The first test was run at 200 A and used an airflow rate of 1100 mls^{-1}. This flow rate was chosen because it was the maximum rate available in the lab and hence provided the highest heat transfer. Fig. 10 shows the temperature profile for Region 9 (the center of the cell) in addition to inlet and outlet temperature data. Battery SOC is also shown on the right axis of Fig. 9. It is seen that the cooling system converges to a steady-state differential of 10 °C between the outlet and inlet air temperatures.

Fig. 10 demonstrates that an air-cooled system utilizing aluminum foam to increase the effective heat transfer coefficient can be used to successfully manage the heat generated by the cells during normal vehicle operation. The maximum temperature recorded in this trial is under 35 °C, which is well within the safe operating range prescribed by the manufacturer. Given the 10 °C temperature rise of the cooling air at steady-state, it can be concluded that this cooling system could limit the battery temperature to 50 °C even at ambient operating temperatures as high as 40 °C. These results support the conclusion that the air-cooled system is an effective solution for maintaining a safe cell

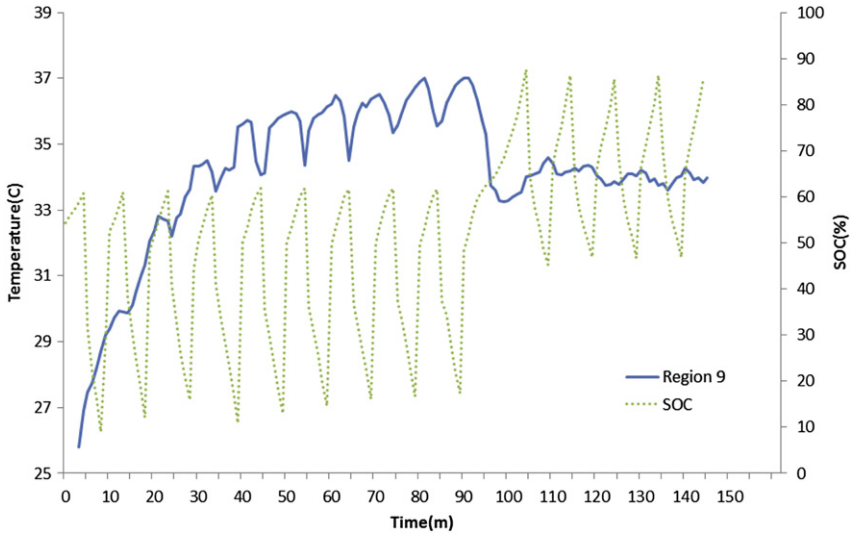

Fig. 9. Temperature (left axis) from the TLC strips at region 9 (See Fig. 4) and battery SOC (right axis) are plotted against time for charge-discharge cycling at 175 A with a coolant airflow rate of 950 mls^{-1} per heat-exchanger plate. The oscillations in the temperature curve during charge and discharge cycles is only apparent at low SOC (up to 90 min), clearly demonstrating the effect of SOC on internal resistance and ultimately battery thermal behavior.

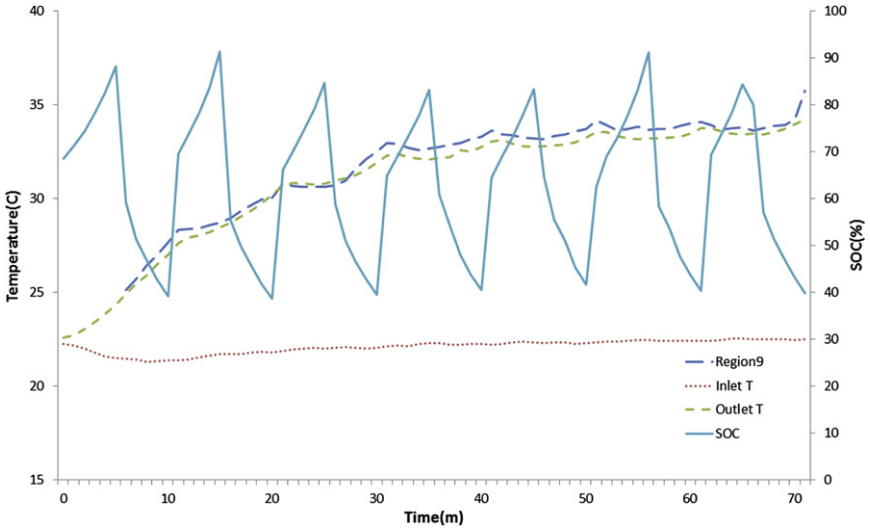

Fig. 10. Temperature at the inlet and outlet thermistor and the temperature at region 9 as measured by the TLC along with battery SOC as a function of time for charge-discharge cycling at 200 A with a coolant airflow rate of 1100 mls^{-1} per heat-exchanger plate. Operating at high SOC suppresses periodic temperature fluctuations leading to consistent steady-state temperature profiles.

operating temperature even under very hot ambient operating conditions with current demands of 200 A.

In addition, another trial was conducted with a reduced coolant airflow rate of 800 mls^{-1} per heat-exchanger plate. Due to the decreased heat transfer coefficient, the steady-state temperature of the cell is expected to increase. These results are shown in Fig. 11. The steady-state differential between the outlet and inlet air temperatures of 14.5 °C indicates that a flow rate of 800 mls^{-1} per heat-exchanger plate can effectively reject the heat generated by the batteries in ambient conditions up to 35 °C. Thus, we arrive at the obvious conclusion that the reduced effective heat transfer coefficient associated with the smaller airflow rate (see Table 1) lowers the maximum allowable ambient operating temperature.

The next test demonstrated the effectiveness of the cooling system at 100 A of charge-discharge cycling employing the original mass flow rate of air of 1100 mls^{-1}. Current demands of this magnitude replicate conditions at the lower end of power demand during vehicle operation. The results from this trial are displayed in Fig. 12. As before, Equation (9) was used to calculate the battery SOC. Note that the temperature from Region 9 does not appear until nearly 40 min into the test because it is below the lowest bandwidth TLC strip which can only register temperatures higher than 25 °C. The results from this test further confirm the feasibility of using ambient air as the active fluid in battery cooling systems.

6. Data analysis

The steady-state temperature results obtained in Section 5 allow a complete thermal analysis of the air-cooled system by applying an energy balance to the cells. The following calculations are presented for the trials that employed an airflow rate of 1100 mls^{-1}. The energy balance calculation is represented by:

$$q_{cell} = q_{plate} + q_{NC} - q_{tabs} \tag{10}$$

where q_{cell} is the heat generated by the cell, q_{tabs} is the heat generated due to contact resistance at the terminals, q_{plate} is the heat removed by the heat exchanger plate and q_{NC} is the heat

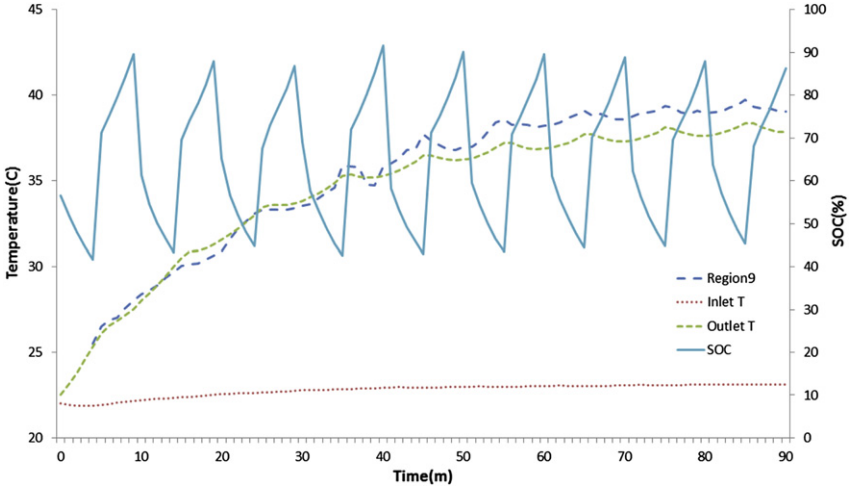

Fig. 11. Temperature and battery SOC as a function of time for charge-discharge cycling at 200 A with a coolant airflow rate of 800 mls^{-1} per heat-exchanger plate. Note that the steady-state temperature rise of the incoming air is 14.5 °C as compared to 10 °C for the flow rate of 1100 mls^{-1}.

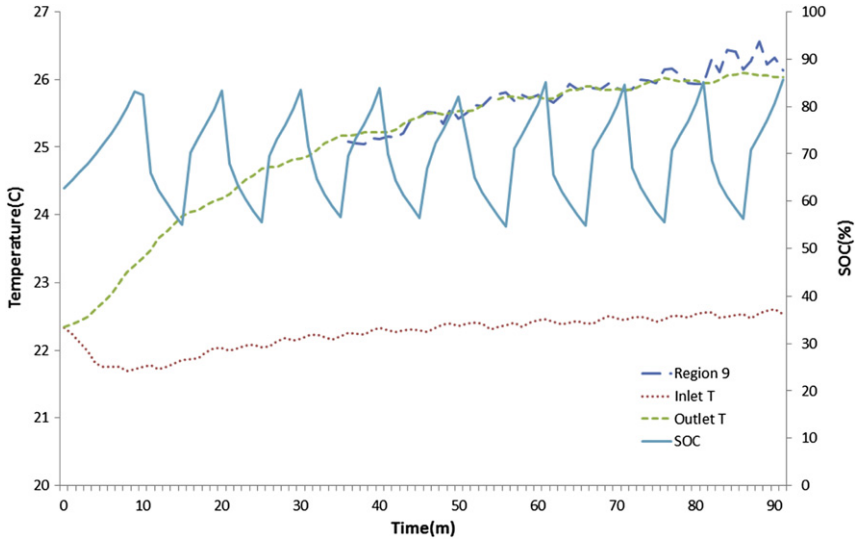

Fig. 12. Temperature and battery SOC as a function of time for charge-discharge cycling at 100 A with a coolant airflow rate of 1100 mls^{-1} per heat-exchanger plate. The system is shown to converge to a steady-state differential of only 4 °C between the outlet and inlet air temperatures.

removed by natural convection. The value of q_{tabs} is known at both 100 and 200 A from [3]. In determining the value of q_{NC} it is important to consider the primary heat removal mechanism. The air-cooled system employed a flow configuration that caused the tab temperatures to be much higher than the water-cooled system used in [3] and therefore one must account for the heat removal by natural convection from the tabs, given as:

$$q_{NC} = hA(T_{tabs} - T_{ambient}) \tag{11}$$

where A is the exposed surface area of the tabs, h is the heat transfer coefficient for natural convection estimated at 5 W m^{-2} K^{-1}, and ΔT is the temperature differential between the terminal and ambient air.

The contribution of the heat exchanger plate was calculated as:

$$q_{plate} = \dot{m}Cp(T_{outlet} - T_{inlet}) \tag{12}$$

where $\dot{m}$ is the mass flow rate of air measured by the rotameter, C_p is the specific heat of air, and the temperature difference represents the rise in air temperature from inlet to outlet. The results from this analysis are shown in Table 2.

In high capacity, high-current cells such as the 50 Ah lithium–titanate batteries studied here, the dominant mechanism of heat generation is ohmic heating due to the electrical resistance as described by Equation (8). Therefore, the values of q_{cell} in Table 2 can be compared directly to the value of heat generated by ohmic losses. Altairnano specifies the internal resistance of a single cell to be 0.00055 Ω. An inspection of Fig. 8 yields a similar value, and most importantly, shows that the value of internal resistance is independent of current direction at high SOC. Equation (5) then yields heat generation values of 22–24 W and 5.5–6 W for current values of 200 A and 100 A, using internal resistance as 0.00055 and 0.0006 Ω respectively. Considering the uncertainty in value of h for natural convection, these values closely match the results shown in Table 2, confirming the validity of the energy balance.

Table 2
Results from the analysis using Equations (10)–(12) giving the relative magnitudes of heat generation and removal terms.

	q_{plate} (W)	q_{NC} (W)	q_{tabs} (W)	q_{cell} (W)
100 A	6	1	0.2	6.8
200 A	16	5	1	20

7. Comparisons to traditional cooling systems

The obvious benefit of the air-cooled system is the elimination of on-board chiller unit and coolant pump leading to savings in parasitic power consumption and weight. As shown in Table 1, the parasitic power consumed by the air-cooled system on a per-plate basis is 5.69 and 2.76 W at 1100 and 800 mls^{-1}, respectively. In comparison, the current cooling system on the University of Delaware's fuel cell bus [7] consists of a 400 W pump and a 1600 W chiller with a 50% duty-cycle during normal ambient conditions. Therefore, the average parasitic loss due to battery thermal management amounts to 1200 W, with a maximum draw of 2000 W. We can compare these values to the data presented in Table 1 by multiplying the computed power value by 264 which represents the number of heat exchanger plates that would be required by the UD fuel cell bus. These values are 1500 W and 730 W for 1100 mls^{-1} and 800 mls^{-1} respectively. Thus, the reduced power consumption for the air-cooled system is encouraging even before considering the benefits of curb weight and cost reduction.

It is also important to consider the effect of an air-cooled system on the volumetric energy density of a battery pack, as this parameter often limits a systems feasibility on a vehicle. The current cooling system on the University of Delaware's fuel cell bus employs heat exchanger plates that measure 4.77 mm in thickness. In order to offer a direct volumetric comparison to the present thermal management system we chose this value as the driving dimension of the aluminum foam insert. The air-cooled system tested in this work also featured 1.27 mm aluminum plates which allowed each heat exchanger plate to be sealed with a weld. A full size scale-up would employ a different method of air sealing, potentially utilizing a gasket material and the cell compression to provide an adequate enclosure. In this scenario, the overall thickness of each heat exchanger plate would remain constant when compared to a traditional cooling system, thus preserving the volumetric energy density of the battery stack.

8. Conclusions

The design, construction, and evaluation of a cooling system for 50 Ah lithium–titanate cells that utilizes ambient air as the active fluid has been described. The key component of the cooling system is a heat exchanger based on open cell aluminum foam to increase

the effective heat transfer coefficient. Experiments indicate that the temperature rise of the battery is restricted to just 10 °C above ambient even under charge-discharge cycling at 200 A. The results indicate that an air-cooled system is a realistic solution for thermal management of these batteries. Moreover, calculations for parasitic power consumption indicate that the energy overhead of such a cooling system is modest, which increases overall vehicle efficiency.

The air-cooled system can benefit from further improvements. For example, a thermostatic control can be implemented to regulate air flow rate based on battery current demand and ambient temperature. Varying the air flow rate as required would further reduce the parasitic power consumption and increase the efficiency of the system, thus making it an attractive option for HEV and BEV applications. It is important to consider that the cells were tested in ambient conditions of 22 °C, leading to significant contributions of natural convection, especially when operating at high currents. If the battery stack was confined to a thermally insulated storage compartment the effect of natural convection would be limited, forcing the cooling system to account for the additional demand. However, these conditions would only be reached in high temperature climates when the cells were operating at 200 A for a prolonged period of time.

This work has demonstrated that ambient air can serve as the active fluid in a thermal management system for high capacity lithium–titanate cells as they undergo the substantial current demands of normal vehicle operation. Eventually, this system can be implemented in real world conditions to increase the overall efficiency of the vehicle while maintaining safe battery operating conditions.

Acknowledgments

This work was funded by a grant from the Federal Transit Administration. We are grateful to Doug Brunner, Stephen Hale and Adam Kinzey for their help with this research.

References

[1] A. Gotcher, Advanced Materials and Processes 163 (12) (2005) 32–38.
[2] 50 Amp Hour Cell (Feb. 1, 2012) [Online Data Sheet] Available: http://www.b2i.cc/Document/546/50Ah_Datasheet-012209.pdf.
[3] M. Giuliano, S. Advani, A. Prasad, Journal of Power Sources 196 (15) (2011) 6517–6524.
[4] Z. Zhang, L. Jia, N. Zhao, L. Yang, Journal of Thermal Science 20 (6) (2011) 570–575.
[5] Flow Resistance of ERG's Reticulated Metal Foams: 20ppi Air at STD Conditions (Dec. 6, 2011) [Online Image] Available: http://www.ergaerospace.com/Pressure-Drop.html.
[6] T.J. Lu, H.A. Stone, M.F. Ashby, Acta Materialia 46 (1998) 3619–3635.
[7] P. Bubna, D. Brunner, S.G. Advani, A.K. Prasad, Journal of Power Sources 195 (19) (2010) 6699–6708.